Entanglement measures in embedding quantum simulators with nuclear spins

Tao Xin,[1,2] Julen S. Pedernales,[3,4] Enrique Solano,[3,5] and Gui-Lu Long[1,2,6,*]

[1]*State Key Laboratory of Low-Dimensional Quantum Physics and Department of Physics, Tsinghua University, Beijing 100084, China*
[2]*Tsinghua National Laboratory of Information Science and Technology, Beijing 100084, China*
[3]*Department of Physical Chemistry, University of the Basque Country UPV/EHU, Apartado 644, 48080 Bilbao, Spain*
[4]*Institute for Theoretical Physics and IQST, Albert-Einstein-Allee 11, Universität Ulm, D-89069 Ulm, Germany*
[5]*IKERBASQUE, Basque Foundation for Science, Maria Diaz de Haro 3, 48013 Bilbao, Spain*
[6]*The Innovative Center of Quantum Matter, Beijing 100084, China*

We implement an embedding quantum simulator (EQS) in nuclear spin systems. The experiment consists of a simulator of up to three qubits, plus a single ancillary qubit, where we are able to efficiently measure the concurrence and the three-tangle of two-qubit and three-qubit systems as they undergo entangling dynamics. The EQS framework allows us to drastically reduce the number of measurements needed for this task, which otherwise would require full-state reconstruction of the qubit system. Our simulator is built of the nuclear spins of four ^{13}C atoms in a molecule of trans-crotonic acid manipulated with NMR techniques.

I. INTRODUCTION

Entanglement, having no classical counterpart, is one of the most distinctive features of quantum mechanics [1,2], and it is considered to be a fundamental resource for quantum information processing and quantum communication [3]. Therefore, it is not surprising that the quantification of entanglement is a major topic for both the theoretical and the experimental quantum information communities. In this respect, entanglement monotones have been introduced as functionals of a quantum state that take a null value for separable states and do not increase under local operations and classical communication [4]. Unfortunately, it is believed that the measurement of entanglement monotones requires, in general, full-state tomography (FST) of the system of interest, something that makes it experimentally intractable in scalable quantum systems, as the number of necessary measurements for FST grows exponentially with the system size [5–7]. For instance, $4^n - 1$ observables need to be measured to reconstruct the wave function of n qubits, which pose a difficulty comparable to the classical simulation of such a wave function with ordinary computers. There have been efforts to circumvent this difficulty. A paradigmatic example is that of "entanglement witnesses" which were introduced as detectors of entanglement. In this case, the value of a physical observable indicates whether an arbitrary quantum state is entangled or not [8]; however, only witnesses for specific kinds of entanglement are known, and not universal ones. Moreover, entanglement witnesses may detect but not quantify, in general, the amount of entanglement and therefore do not serve as a comparative tool among different entangled states. Other alternative methods rely on collective measurements on many identical copies of a given quantum state, which is experimentally demanding as well [9,10]. On the other hand, it is known that FST is necessary for universal entanglement detection with single-copy observables [11]. All in all, quantum computers and quantum simulators do not seem *a priori* to be efficient tools for the quantification of entanglement, at least when compared to classical computers.

Embedding quantum simulators (EQSs) [12,13] have been proposed as a path to solve this conflict in the context of scalable quantum platforms. A one-to-one quantum simulator, which directly implements the wave function of interest and its dynamics in a controllable quantum system, is bound to direct detection of the entanglement present on it, if it measures the entanglement of the system that it simulates. However, in many situations, one is not necessarily interested in the entanglement present in the physical system but rather in the entanglement predicted by the simulated model and its evolution in time, in the same manner that the numerical simulation of quantum systems is not concerned about the inexistent entanglement among the classical bits employed for the simulation. Therefore, a suitable mapping of the model of interest to the quantum simulator that exposes the entanglement of the simulated system without the necessity of FST is of interest. EQSs provide a systematic manner to construct quantum simulators on which entanglement monotones are accessible with a reduced number of measurements when compared to FST. This is done by the addition of a single ancillary qubit and a suitable mapping of the initial state and the Hamiltonian dynamics that allows for the measurement of antilinear operators.

In this work, we show the first implementation of the EQS framework with nuclear spins. We implement two EQSs: first a simulator of two qubits implemented with three nuclear spins, and second a three-qubit quantum simulator built of four nuclear spins. For the two-qubit simulator we measure the concurrence of the system as it evolves under an entangling

*Correspondence and requests for materials should be addressed to: gllong@tsinghua.edu.cn

Hamiltonian. We do this with the measurement of just 2 observables, as opposed to the 15 needed for FST. In the second case, we measure the three-tangle of the system, which is an entanglement monotone that detects genuine tripartite entanglement in a three-qubit system. In this case, the necessary observables are reduced from the 63 needed for full-state reconstruction to only 6 observables.

II. EQS AND ENTANGLEMENT MONOTONES

For a given Hamiltonian of interest, we assume a matrix representation that can be decomposed in its real and imaginary parts as $H = A + iB$, where A and B are real matrices, which are respectively Hermitian, $A = A^\dagger$, and anti-Hermitian, $B = -B^\dagger$. If we consider an arbitrary initial state $|\phi(0)\rangle$, a one-to-one quantum simulator would directly implement it in a physical system and evolve it under Hamiltonian H. In contrast, an EQS implements it in an enlarged Hilbert space onto which both the initial state and the Hamiltonian are mapped. The initial state is mapped as $|\Phi(0)\rangle = |0\rangle \otimes \mathrm{Re}|\phi(0)\rangle + |1\rangle \otimes \mathrm{Im}|\phi(0)\rangle$ and the Hamiltonian as $H' = i\sigma_0 \otimes B - \sigma_y \otimes A$, where σ_0 is a 2×2 identity matrix and $\sigma_{x,y,z}$ are Pauli matrices. Under this mapping, which only requires the addition of one ancillary qubit, regardless of the size of the simulated system, expectation values of antilinear operators can be retrieved with the measurement of two observables. Antilinear operators take the form OK, where O is an observable and K is the complex conjugation operator, which acts on the vector elements of a ket state by complex conjugating them, $K|\phi\rangle = |\phi^*\rangle$. Antilinear operators are not Hermitian and therefore they are not observables, generally requiring full-state reconstruction of the quantum state of a system to compute their expectation value. However, under the mapping introduced above, antilinear operators can be efficiently computed in an EQS according to the relation

$$\langle\phi(t)|O|\phi^*(t)\rangle = \langle\Phi(t)|\sigma_z \otimes O|\Phi(t)\rangle - i\langle\Phi(t)|\sigma_x \otimes O|\Phi(t)\rangle. \quad (1)$$

It is known that entanglement monotones for qubit systems can be systematically constructed from antilinear operators [14]. For instance, the concurrence, which is a two-qubit entanglement monotone, can be represented as $\mathcal{C} = \langle\phi(t)|\sigma_y \otimes \sigma_y|\phi^*(t)\rangle$. In an embedding quantum simulator, this would be retrieved from the expectation values of observables $\sigma_z\sigma_y\sigma_y$ and $\sigma_x\sigma_y\sigma_y$ in the enlarged space,
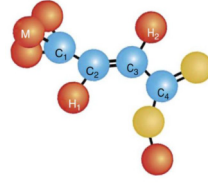
$$\mathcal{C} = |\langle\sigma_z \otimes \sigma_y \otimes \sigma_y\rangle - i\langle\sigma_x \otimes \sigma_y \otimes \sigma_y\rangle|, \quad (2)$$

reducing the number of required observables to 2, from the 15 required to do FST of a two-qubit system.

As another paradigmatic example, we can mention the three-qubit entanglement monotone three-tangle, which can be defined in terms of antilinear operators as

$$\mathcal{E}_3 = |-\langle O_1 K\rangle^2 + \langle O_2 K\rangle^2 + \langle O_3 K\rangle^2|, \quad (3)$$

with $O_1 = \sigma_0\sigma_y\sigma_y$, $O_2 = \sigma_x\sigma_y\sigma_y$, and $O_3 = \sigma_z\sigma_y\sigma_y$. Each of the antilinear operators can be mapped onto two Hermitian operators in the EQS, which makes the three-tangle accessible with the measurement of just 6 observables, as opposed to the

FIG. 1. Molecular structure and Hamiltonian parameters of ^{13}C-labeled trans-crotonic acid. In experiments, C1, C2, C3, and C4 are used as a four-qubit simulator. In the table, the chemical shifts and J-couplings (in Hz) are presented by the diagonal and off-diagonal elements, respectively. The last row of the table shows T_2 (in seconds).

	C1	C2	C3	C4
C1	-1705.5			
C2	41.64	-14558.1		
C3	1.48	69.78	-12330.5	
C4	7.06	1.18	72.36	-16764.1
T2	1.02	0.92	0.87	0.94

63 required to do FST of three qubits: $\sigma_z\sigma_0\sigma_y\sigma_y$, $\sigma_x\sigma_0\sigma_y\sigma_y$, $\sigma_z\sigma_x\sigma_y\sigma_y$, $\sigma_x\sigma_x\sigma_y\sigma_y$, $\sigma_z\sigma_z\sigma_y\sigma_y$, and $\sigma_x\sigma_z\sigma_y\sigma_y$.

III. EXPERIMENTAL REALIZATION IN NMR

For a proof-of-principle demonstration of EQSs in spin systems, we choose a platform of verified controllability and precision like NMR [15]. Although the potentiality of NMR platforms to scale up to relevant system sizes is unclear, it is important to demonstrate the working principles of EQSs in spin systems. This opens the door to the implementation of EQSs in other more scalable spin-based quantum platforms that are as well manipulated with NMR or analogous techniques. This include nitrogen-vacancy (NV) centers in diamond crystals [16], hyperfine-qubits in ion traps [17,18], or color centers in two-dimensional materials [19].

In our experiment, we have used four qubits in a sample of ^{13}C-labeled trans-crotonic acid dissolved in d6-acetone. The four-qubit quantum simulator is implemented with the nuclear spins of four carbon atoms of the trans-crotonic acid molecule labeled from C1 to C4, after canceling their coupling to the methyl group M and to the hydrogen atoms labeled H1 and H2. In Fig. 1 we give a pictorial representation of the molecular structure together with the values of some relevant parameters. All experiments were carried out on a Bruker AVANCE 400-MHz spectrometer at room temperature. The Hamiltonian of our system under the weak coupling approximation can be written as

$$\mathcal{H}_{\mathrm{int}} = \sum_{j=1}^{4} \pi(\nu_j - \nu_0)\sigma_z^j + \sum_{j<k,=1}^{4} \frac{\pi}{2} J_{jk}\sigma_z^j\sigma_z^k, \quad (4)$$

where ν_j and J_{jk} are the chemical shifts and the J-coupling strengths, respectively. ν_0 is the reference frequency of the ^{13}C channel in the NMR platform.

We initialize the system in a pseudopure state (PPS), which is the pure state of interest $|0000\rangle$ only with probability ϵ and a maximally mixed state otherwise. This is represented with the density matrix $\rho_{0000} = (1 - \epsilon)\sigma_0^{\otimes 4}/16 + \epsilon|0000\rangle\langle0000|$, where the polarization ϵ takes the value $\epsilon = 10^{-5}$ in our experiment. Conveniently enough, the expectation value of any observable measured for such a state will be that corresponding to the state $|0000\rangle$ and its time evolution, as the identity part of the state does not evolve nor contribute to the NMR signals. To generate this PPS from the initial thermal state, we used the spatial averaging technique [20–22] and then
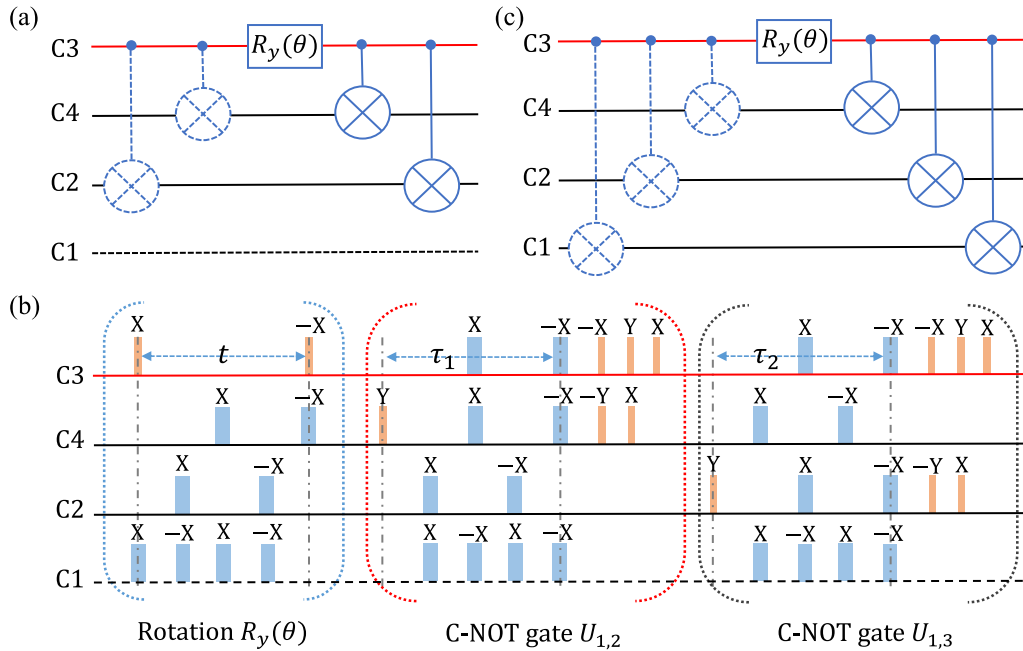
FIG. 2. Quantum circuit and corresponding NMR pulse sequence. (a) Quantum circuit consisting of four controlled-NOT gates and one local rotation $R_y(\theta)$, which implements the evolution associated with the Hamiltonian $H = -\omega\, \sigma_y \otimes \sigma_x \otimes \sigma_x$. The upper (red) line represents the ancillary qubit in the EQS, which is held by the nuclear spin of atom C3. Black solid and dashed lines represent the work and idle qubits, respectively. The dotted controlled-NOT gates can be avoided for initial states of the form $|0000\rangle$. (b) NMR pulse sequence corresponding to the circuit in panel (a). The orange and blue rectangles represent, respectively, $\pi/2$ and π pulses around the directions indicated on top of them. Parameters τ_1 and τ_2 take values $\tau_1 = 1/2J_{C3,C4}$ and $\tau_2 = 1/2J_{C3,C2}$. (c) Quantum circuit for the implementation of the Hamiltonian $H = -\omega\, \sigma_y \otimes \sigma_x \otimes \sigma_x \otimes \sigma_x$, consisting of six controlled-NOT gates and one local rotation $R_y(\theta)$.

performed FST [23,24] to benchmark the quality of our PPS. A fidelity of 98.77% is computed between the target pure state $|0000\rangle\langle 0000|$ and the experimentally sensitive part of the constructed PPS, setting the ground for reliable subsequent simulations.

For a first experiment, we consider a small toy model consisting of the two-qubit initial state $|\phi_2(0)\rangle = |00\rangle$ evolving under the entangling Hamiltonian ($\hbar = 1$) $H_2 = \omega\sigma_x \otimes \sigma_x$. The common method to track the evolution of concurrence for such a small model would involve performing FST of the evolved state $|\phi_2(t)\rangle = e^{-iH_2t}|00\rangle$ at a collection of times t_i, which would require the measurement of 15 observables at each time t_i. Then with the whole wave function concurrence would be computed according to $\mathcal{C} = |\langle\phi(t)|\sigma_y \otimes \sigma_y|\phi^*(t)\rangle|$, which for this specific system can be shown to be $\mathcal{C} = |\sin 2\omega t|$.

Using the EQS formalism, the problem is recast into the initial state $|\Phi_2(0)\rangle = |000\rangle$ evolving under the Hamiltonian $\tilde{H}_2 = -\omega\sigma_y \otimes \sigma_x \otimes \sigma_x$. In Fig. 2(a), we show the quantum circuit that implements such an evolution, which includes four controlled-NOT gates and one local rotation $R_y(\theta) = \exp(-i\theta\sigma_y/2)$ acting on the ancillary qubit with $\theta = -2\omega t$. Considering that the initial state $|000\rangle$ is unaffected by the first two controlled-NOT gates, one can reduce the circuit to that one indicated by the continuous lines in Fig. 2(a), disregarding the diagram parts represented with discontinuous lines. Controlled-NOT gates $U_{a,b}$, with qubit a and b representing the control and target qubits, respectively, can be decomposed into a suitable form for their implementation in NMR, consisting

of local rotations and J-coupling kind evolutions [25]:

$$U_{a,b} = \sqrt{i}\, R_z^a\left(\frac{\pi}{2}\right) R_z^b\left(-\frac{\pi}{2}\right) R_x^b\left(\frac{\pi}{2}\right) U\left(\frac{1}{2J}\right) R_y^b\left(\frac{\pi}{2}\right). \quad (5)$$

Here, $U(\frac{1}{2J})$ is the J-coupling evolution $e^{-i\pi\sigma_z^a\sigma_z^b/4}$. Moreover, any z-rotation $R_z(\theta)$ can be decomposed in terms of rotations around the x and y axes, $R_z(\theta) = R_y(\pi/2)R_x(-\theta)R_y(-\pi/2)$. Local rotations $R_y(\theta)$ can be realized by setting the reference frequency ν_0 to satisfy the condition $\nu_3 - \nu_0 = -50$ Hz and using refocusing pulses to cancel the phase accumulated on the unaddressed ^{13}C because of the offset [26]. The specific pulse sequence consisting exclusively of local rotations and J-coupling evolutions is illustrated in Fig. 2(b). Because selective excitations are usually imperfect in homonuclear systems and the effect of too many pulses is accumulative, resulting in a snowball effect of imprecisions, we choose to pack up all the pulses together and implement the simulation via the gradient ascent pulse engineering (GRAPE) technique [27,28]. The GRAPE approach provides a 15-ms shaped-pulse width and over 99.5% fidelity for the whole package of pulses.

In our setup, we can measure expectation values of observables of the forms $\sigma_{x,y} \otimes \sigma_{0,z}^{\otimes n-1}$ and $\sigma_{x,y} \otimes |k\rangle\langle k|^{\otimes n-1}$ by measuring the free induction decay (FID) signal at the end of the protocol (see Appendix B). Here, n is the total number of system qubits and k can take values 0 and 1. For the simulation of this first model, we only need three physical qubits. Therefore, we leave qubit C4 as a spectator qubit that does not take part in the dynamics, as indicated in Fig. 2, and we handle the data in the subspace associated with the initial state
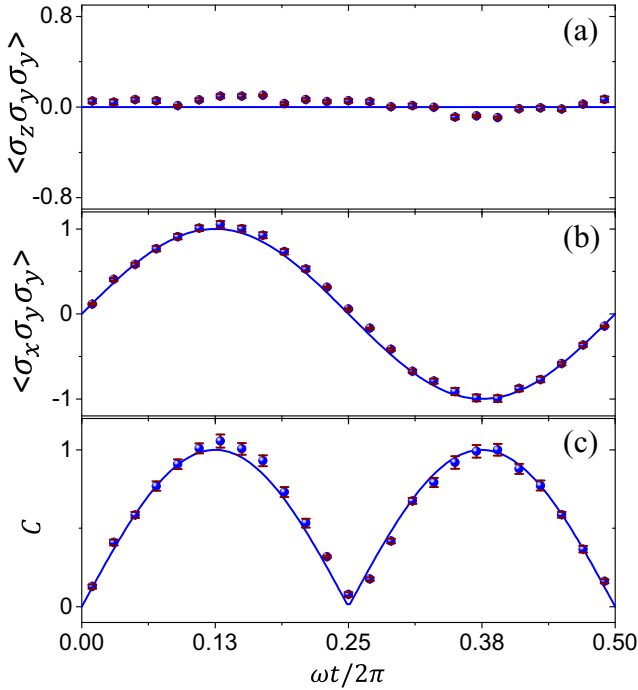
FIG. 3. Experimental results for the evolution of concurrence, $\mathcal{C}(t)$. Panels (a) and (b) show the time evolution of the expectation values of the EQS observables $\sigma_z\sigma_y\sigma_y$ and $\sigma_x\sigma_y\sigma_y$, respectively. (c) Reconstructed concurrence $\mathcal{C}(t)$ of the simulated model from the values of the measured $\langle\sigma_z\sigma_y\sigma_y\rangle$ and $\langle\sigma_x\sigma_y\sigma_y\rangle$. The dots represent experimental data and the lines stem from theory predictions. The error bars are calculated from the estimated imperfections of the GRAPE pulses, PPS preparation, and T_2-decoherence effects.

$|0\rangle$ of qubit C4. This means that the two observables of interest, $\sigma_z\sigma_y\sigma_y$ and $\sigma_x\sigma_y\sigma_y$, are retrieved from the expectation values of the four-qubit operators $\sigma_z\sigma_y\sigma_y \otimes |0\rangle\langle0|$ and $\sigma_x\sigma_y\sigma_y \otimes |0\rangle\langle0|$. We consider 25 temporal points ranging from $\omega t_{\text{in}}/2\pi = 0.01$ to $\omega t_{\text{f}}/2\pi = 0.49$ with steps of $\omega t_{\text{st}}/2\pi = 0.02$. For each time t_i, we carry out the evolution of the EQS twice, and we measure after each of the evolutions the expectation value of one of the observables, $\langle\sigma_z\sigma_y\sigma_y\rangle$ or $\langle\sigma_x\sigma_y\sigma_y\rangle$ (see Appendix A). The results and their comparison to theoretical predictions are shown in Fig. 3.

We consider a somewhat more involved case now with the simulation of a three-qubit entangling dynamics, which consists of the initial state $|\phi_3(0)\rangle = |000\rangle$ evolving under the Hamiltonian $H_3 = \omega\, \sigma_x \otimes \sigma_x \otimes \sigma_x$. Following the same recipe introduced in the analysis of the previous case, the EQS for such a model consists of the Hamiltonian $\tilde{H}_3 = -\omega\, \sigma_y \otimes \sigma_x \otimes \sigma_x \otimes \sigma_x$ acting on the initial state $|\Phi_4(0)\rangle = |0000\rangle$. Figure 2(c) illustrates the corresponding quantum circuit, which includes six controlled-NOT gates and a local operation $R_y(\theta) = \exp(-i\theta\sigma_y/2)$, with $\theta = -2\omega t$, acting on the ancillary qubit. Based on the same considerations as those of the previous experiment, the first three controlled-NOT gates can be disregarded and the remaining pulse sequence packed up and implemented with the GRAPE technique, which for this case results in a 30-ms shaped-pulse with over 99.5% fidelity. Then, we measure the expectation value of the six observables of interest: $\sigma_z\sigma_0\sigma_y\sigma_y$, $\sigma_x\sigma_0\sigma_y\sigma_y$, $\sigma_z\sigma_x\sigma_y\sigma_y$, $\sigma_x\sigma_x\sigma_y\sigma_y$,

$\sigma_z\sigma_z\sigma_y\sigma_y$, and $\sigma_x\sigma_z\sigma_y\sigma_y$ (see Appendix A). We consider the same temporal points as those of the previous experiment. In Fig. 4, we presents the results of these experiments and the corresponding three-tangle $\mathcal{E}_3$ computed with them.

IV. DISCUSSION AND CONCLUSION

It is believed that liquid state NMR platforms present little or no entanglement among their computational degrees of freedom, however, they still serve as a rather stable and highly controllable quantum platform, where unitary evolutions can be implemented, at least in a small scale. In this respect, the demonstration of algorithms in NMR serves as a test bed for the implementation of such protocols in other spin-based quantum platforms, where the physics and control techniques are assumed to be similar. Here, we have demonstrated the feasibility of EQSs with nuclear spins manipulated via NMR techniques, something fundamentally different from previous photonic implementations of EQSs and that could open the door to their implementation in presumably more scalable spin-based quantum platforms, like NV centers or microwave trapped ions. In particular, we have employed a four-qubit NMR platform to compute the evolution of entanglement on a simulated three-body system. Notice that our approach does not measure the entanglement present in the system, if any, but it rather computes the entanglement in the simulated system.

For the mixed-state case the standard definition of entanglement monotones invokes the convex roof $E(\rho) = \min \sum_i p_i E(|\phi_i\rangle)$, where the minimum is taken over the infinite pure-state decompositions $(p_i, |\phi_i\rangle)$ of ρ. In this respect, an EQS could be combined with classical means to provide a quantum-classical hybrid algorithm, where an EQS would be employed to compute the entanglement monotones associated with the pure states in each decomposition, $E(|\phi_i\rangle)$. This information would be fed to a classical machine running a minimization algorithm, which would indicate which decomposition to try next until a minimum is found [12].

If scalable quantum simulators and quantum computers are to be used as tools in the analysis of entanglement and its dynamics, they will unavoidably need to be designed under suitable mappings that guarantee that entanglement measures can be efficiently retrieved. The EQS paradigm offers a mapping which drastically reduces the number of observables that codify this information, with a minimum added complexity in the initialization and dynamics of the quantum simulator. Here, we validate these ideas with two experiments in nuclear spins controlled with NMR techniques. Our experimental results show a high degree of correspondence with the theory predictions, opening the door to the experimental field of EQSs in spin-based platforms.
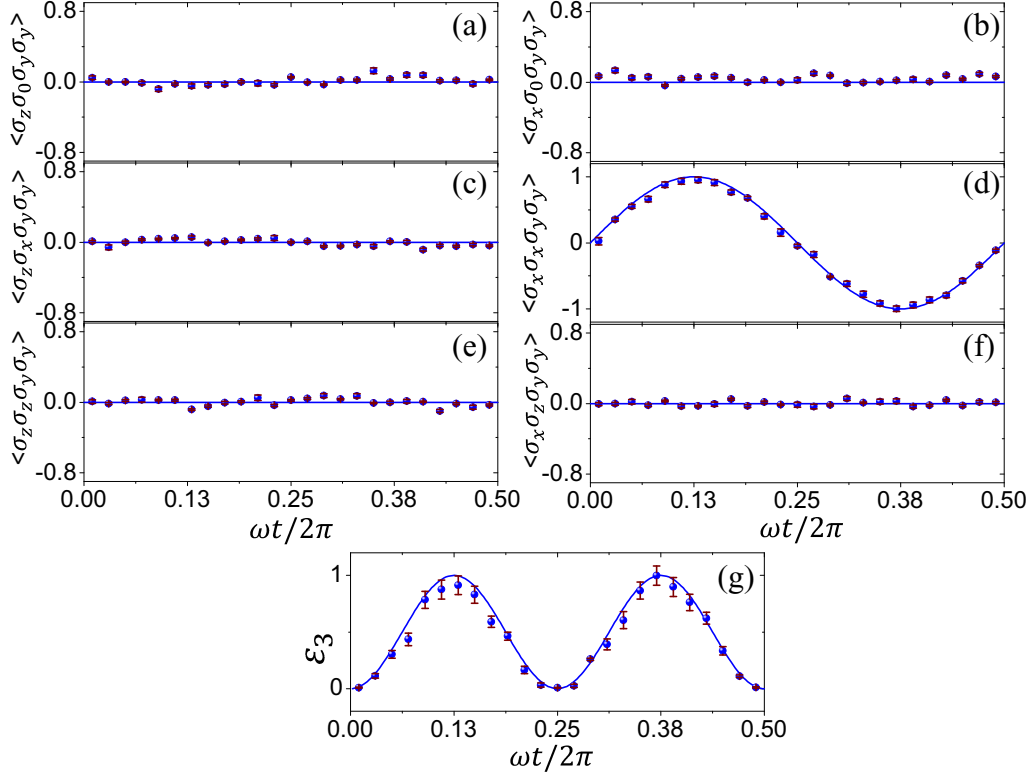
FIG. 4. Experimental results for the evolution of the three-tangle $\mathcal{E}_3$. Panels (a)–(f) show the expectation values of observables $\sigma_z\sigma_0\sigma_y\sigma_y$, $\sigma_x\sigma_0\sigma_y\sigma_y$, $\sigma_z\sigma_x\sigma_y\sigma_y$, $\sigma_x\sigma_x\sigma_y\sigma_y$, $\sigma_z\sigma_z\sigma_y\sigma_y$, and $\sigma_x\sigma_z\sigma_y\sigma_y$, respectively. Panel (g) provides the result of the time evolution of the three-tangle $\mathcal{E}_3(t)$ computed from the measurements of the previous six observables. The dots are experimental points and the lines are theory predictions. The error bars are estimated from the noise introduced by the GRAPE pulses, imperfect PPS preparation, and the T_2-decoherence effect.

APPENDIX A: MEASUREMENT OF THE OBSERVABLES

In the first case explored in the main text, the two observables of interest, $\sigma_z\sigma_y\sigma_y$ and $\sigma_x\sigma_y\sigma_y$, are retrieved from the expectation values of the four-qubit operators $\sigma_z\sigma_y\sigma_y \otimes |0\rangle\langle 0|$ and $\sigma_x\sigma_y\sigma_y \otimes |0\rangle\langle 0|$. In order to measure these operators, we perform rotations $\{YXXI, IXXI\}$ before the measurement of the FID signal, which results in the following transformations:

$$\sigma_z\sigma_y\sigma_y \otimes |0\rangle\langle 0| \xrightarrow{YXXI} \sigma_x\sigma_z\sigma_z \otimes |0\rangle\langle 0|,$$
$$\sigma_x\sigma_y\sigma_y \otimes |0\rangle\langle 0| \xrightarrow{IXXI} \sigma_x\sigma_z\sigma_z \otimes |0\rangle\langle 0|, \quad \text{(A1)}$$

where $X = \exp(-i\sigma_x\pi/4)$ and $Y = \exp(-i\sigma_y\pi/4)$. In this manner, the expectation values of interest are directly obtained from the experimental spectrum. The pulses corresponding to these last rotations in the measurement process are again realized using the GRAPE technique, which in this case results in a 1-ms shaped-pulse of fidelity 99.5%.

For the second experiment, we need to measure the expectation value of the six observables of interest, $\sigma_z\sigma_0\sigma_y\sigma_y$, $\sigma_x\sigma_0\sigma_y\sigma_y$, $\sigma_z\sigma_x\sigma_y\sigma_y$, $\sigma_x\sigma_x\sigma_y\sigma_y$, $\sigma_z\sigma_z\sigma_y\sigma_y$, and $\sigma_x\sigma_z\sigma_y\sigma_y$, to reconstruct the three-tangle $\mathcal{E}_3$. For these, and in a fashion similar to the procedure followed in the previous experiment, we transform our final state under the rotations $\{IIXX, YIXX, Y\bar{Y}XX, I\bar{Y}XX\}$ in order to map the expectation values of interest to the measured FID signal at the end of

the protocol:

$$\sigma_x\sigma_0\sigma_y\sigma_y, \sigma_x\sigma_z\sigma_y\sigma_y \xrightarrow{IIXX} \sigma_x\sigma_0\sigma_z\sigma_z, \sigma_x\sigma_z\sigma_z\sigma_z,$$
$$\sigma_z\sigma_0\sigma_y\sigma_y, \sigma_z\sigma_z\sigma_y\sigma_y \xrightarrow{YIXX} \sigma_x\sigma_0\sigma_z\sigma_z, \sigma_x\sigma_z\sigma_z\sigma_z,$$
$$\sigma_z\sigma_x\sigma_y\sigma_y \xrightarrow{Y\bar{Y}XX} \sigma_x\sigma_z\sigma_z\sigma_z,$$
$$\sigma_x\sigma_x\sigma_y\sigma_y \xrightarrow{I\bar{Y}XX} \sigma_x\sigma_z\sigma_z\sigma_z. \quad \text{(A2)}$$

Here, $\bar{Y} = \exp(i\sigma_y\pi/4)$ and I is the identity operation. The GRAPE technique is as well used to implement this last sequence of pulses by applying a 1-ms shaped-pulse with a fidelity of 99.5%.

APPENDIX B: MEASUREMENT OF n-BODY SPIN OPERATORS

The FID signal of a four-qubit NMR system contains eight peaks, with the mth peak encoding the expectation values of operators

$$\mathcal{M}_x^m = \sigma_x \otimes |b(m-1)\rangle\langle b(m-1)| \quad \text{and}$$
$$\mathcal{M}_y^m = \sigma_y \otimes |b(m-1)\rangle\langle b(m-1)|, \quad \text{(B1)}$$

where $b(m-1)$ is the binary representation of number $m-1$ in three bits. The expectation value of any tensor product of Pauli matrices can be reconstructed by suitably combining the expectation values of different M_x^m and M_y^m. For instance, the
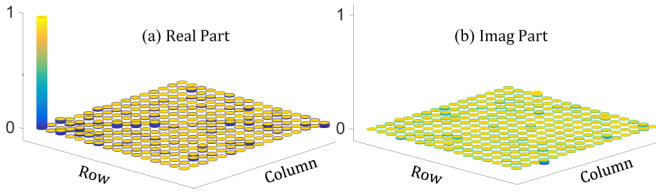
FIG. 5. Real and imaginary parts of the reconstructed PPS matrix. Panels (a) and (b) respectively show the real and imaginary elements of the PPS matrix reconstructed in the experiments. The x and y axes represent the index number of the row and columns of the PPS matrix from 1 to 16. The z axis shows the value of each element of the PPS matrix.

four-qubit operator $\sigma_x\sigma_z\sigma_z\sigma_z$ can be constructed as

$$\sigma_x\sigma_z\sigma_z\sigma_z = \frac{1}{8}\sigma_x \otimes (|0\rangle\langle 0| - |1\rangle\langle 1|)^{\otimes 3} \quad \text{(B2)}$$
$$= \frac{1}{8}\big(M_x^1 - M_x^2 - M_x^3$$
$$+ M_x^4 - M_x^5 + M_x^6 + M_x^7 - M_x^8\big).$$

Other n-body spin operators can be measured in a similar way.

APPENDIX C: TOMOGRAPHY FOR PPS

FST was performed to evaluate the quality of our PPS. Figure 5 shows the reconstructed real and imaginary parts of the PPS density matrix, where only the deviation of the

state from the maximally mixed part is detectable. From these measurements, we found that the fidelity between the target pure state $|0000\rangle\langle 0000|$ and the experimentally sensitive part of the constructed PPS is about 98.77%.

APPENDIX D: COMPUTATION OF THE ERROR BARS

In small scale experimental setups, a good characterization of the error sources can be useful to estimate the confidence interval of the measured expectation values, with a reduced number of experimental runs. In this respect, we follow a standard procedure that goes as follows. For each experimental realization, we numerically simulate the GRAPE pulse including a good decoherence model of our qubits. We compare the expectation values computed in this manner with the measured ones. From their discrepancy, which on average was found to be of 2.71% for the three-qubit simulator and 2.35% for the four-qubit one, plus the 1.30% error associated with the infidelity of the initial state preparation, we estimate bounds for the experimental error of each point. We then assume a Gaussian distribution that will yield values inside these bounds with a 95% probability and we give the error bars of each point associated with the width of this Gaussian distribution.

For experiments of bigger size, where the numerical simulation of the experiment cannot be of assistance in computing the error bars, one would increase the number of experimental runs in order to have a statistically significant amount of data from which a reliable value of the variance could be computed.

[1] L. Amico, R. Fazio, A. Osterloh, and V. Vedral, Rev. Mod. Phys. **80**, 517 (2008).

[2] R. Horodecki, P. Horodecki, M. Horodecki, and K. Horodecki, Rev. Mod. Phys. **81**, 865 (2009).

[3] M. A. Nielsen and I. Chuang, *Quantum Computation and Quantum Information* (Cambridge University, Cambridge, England, 2000).

[4] G. Vidal, J. Mod. Opt. **47**, 355 (2000).

[5] M. Cramer, M. B. Plenio, S. T. Flammia, R. Somma, D. Gross, S. D. Bartlett, O. Landon-Cardinal, D. Poulin, and Y.-K. Liu, Nat. Commun. **1**, 149 (2010).

[6] T. Jullien, P. Roulleau, B. Roche, A. Cavanna, Y. Jin, and D. Glattli, Nature (London) **514**, 603 (2014).

[7] T. Xin, D. Lu, J. Klassen, N. Yu, Z. Ji, J. Chen, X. Ma, G.-L. Long, B. Zeng, and R. Laflamme, Phys. Rev. Lett. **118**, 020401 (2017).

[8] H. S. Park, S. S. B. Lee, H. Kim, S. K. Choi, and H. S. Sim, Phys. Rev. Lett. **105**, 230404 (2010).

[9] F. A. Bovino, G. Castagnoli, A. Ekert, P. Horodecki, C. M. Alves, and A. V. Sergienko, Phys. Rev. Lett. **95**, 240407 (2005).

[10] M. Huber, F. Mintert, A. Gabriel, and B. C. Hiesmayr, Phys. Rev. Lett. **104**, 210501 (2010).

[11] D. Lu, T. Xin, N. Yu, Z. Ji, J. Chen, G.-L. Long, J. Baugh, X. Peng, B. Zeng, and R. Laflamme, Phys. Rev. Lett. **116**, 230501 (2016).

[12] R. Di Candia, B. Mejia, H. Castillo, J. S. Pedernales, J. Casanova, and E. Solano, Phys. Rev. Lett. **111**, 240502 (2013).

[13] J. C. Loredo, M. P. Almeida, R. Di Candia, J. S. Pedernales, J. Casanova, E. Solano, and A. G. White, Phys. Rev. Lett. **116**, 070503 (2016).

[14] A. Osterloh and J. Siewert, Phys. Rev. A **72**, 012337 (2005).

[15] J. A. Jones, V. Vedral, A. Ekert, and G. Castagnoli, Nature **403**, 869 (2000).

[16] M. W. Doherty, N. B. Manson, P. Delaney, F. Jelezko, J. Wrachtrup, and L. C. L. Hollenberg, Phys. Rep. **528**, 1 (2013).

[17] D. Leibfried, R. Blatt, C. Monroe, and D. Wineland, Rev. Mod. Phys. **75**, 281 (2003).

[18] J. S. Pedernales, R. Di Candia, P. Schindler, T. Monz, M. Hennrich, J. Casanova, and E. Solano, Phys. Rev. A **90**, 012327 (2014).

[19] M. Abdi, M.-J. Hwang, M. Aghtar, and M. B. Plenio, Phys. Rev. Lett. **119**, 233602 (2017).

[20] D. G. Cory, A. F. Fahmy, and T. F. Havel, Proc. Natl. Acad. Sci. USA **94**, 1634 (1997).

[21] D. G. Cory, M. D. Price, and T. F. Havel, Phys. D **120**, 82 (1998).

[22] D. Lu, N. Xu, R. Xu, H. Chen, J. Gong, X. Peng, and J. Du, Phys. Rev. Lett. **107**, 020501 (2011).

[23] G. M. Leskowitz and L. J. Mueller, Phys. Rev. A **69**, 052302 (2004).

[24] J.-S. Lee, Phys. Lett. A **305**, 349 (2002).

[25] T. Xin, H. Li, B.-X. Wang, and G.-L. Long, Phys. Rev. A **92**, 022126 (2015).

[26] M. R. Bendall and R. E. Gordon, J. Magn. Reson. **53**, 365 (1983).

[27] N. Khaneja, T. Reiss, C. Kehlet, T. Schulte-Herbruggen, and S. J. Glaser, J. Magn. Reson. **172**, 296 (2005).

[28] C. A. Ryan, C. Negrevergne, M. Laforest, E. Knill, and R. Laflamme, Phys. Rev. A **78**, 012328 (2008).